Received: 6 September 2021 | Revised: 29 December 2021 | Accepted: 30 December 2021

DOI: 10.1002/nbm.4690

RESEARCH ARTICLE

NMR IN BIOMEDICINE WILEY

Assessment of iron nanoparticle distribution in mouse models using ultrashort-echo-time MRI

Andreas Boss[1] | Laura Heeb[2] | Divya Vats[3] | Fabian H. L. Starsich[4,5] | Alice Balfourier[4,5] | Inge K. Herrmann[4,5] | Anurag Gupta[2]

[1]Institute of Diagnostic and Interventional Radiology, University Hospital Zurich, Zurich, Switzerland

[2]Division of Visceral Surgery, University Hospital Zurich, Zurich, Switzerland

[3]D-HEST, ETH Zurich, Zurich, Switzerland

[4]Laboratory for Particles-Biology Interactions, Swiss Federal Laboratories for Materials Science and Technology (Empa), St. Gallen, Switzerland

[5]Department of Mechanical and Process Engineering, ETH Zurich, Nanoparticle Systems Engineering Laboratory, Zurich, Switzerland

Correspondence
Andreas Boss, MD PhD, Institute for Diagnostic and Interventional Radiology, University Hospital of Zurich, Rämistrasse 100, 8091 Zürich, Switzerland.
Email: andreas.boss@usz.ch

Microscopic magnetic field inhomogeneities caused by iron deposition or tissue-air interfaces may result in rapid decay of transverse magnetization in MRI. The aim of this study is to detect and quantify the distribution of iron-based nanoparticles in mouse models by applying ultrashort-echo-time (UTE) sequences in tissues exhibiting extremely fast transverse relaxation. In 24 C57BL/6 mice (two controls), suspensions containing either non-oxidic Fe or $AuFeO_x$ nanoparticles were injected into the tail vein at two doses (200 μg and 600 μg per mouse). Mice underwent MRI using a UTE sequence at 4.7 T field strength with five different echo times between 100 μs and 5000 μs. Transverse relaxation times T_2^* were computed for the lung, liver, and spleen by mono-exponential fitting. In UTE imaging, the MRI signal could reliably be detected even in liver parenchyma exhibiting the highest deposition of nanoparticles. In animals treated with Fe nanoparticles (600 μg per mouse), the relaxation time substantially decreased in the liver (3418 ± 1534 μs (control) versus 228 ± 67 μs), the spleen (2170 ± 728 μs versus 299 ± 97 μs), and the lungs (663 ± 101 μs versus 413 ± 99 μs). The change in transverse relaxation was dependent on the number and composition of the nanoparticles. By pixel-wise curve fitting, T_2^* maps were calculated showing nanoparticle distribution. In conclusion, UTE sequences may be used to assess and quantify nanoparticle distribution in tissues exhibiting ultrafast signal decay in MRI.

KEYWORDS
iron quantification, nanoparticle, ultrashort-echo-time, UTE

1 | INTRODUCTION

Among the broad spectrum of nanoparticles available for biomedical applications, iron-based nanoparticles have attracted significant attention due to their unique magnetic properties and excellent biocompatibility. These attributes render them highly promising for various therapeutic (eg magnetic particle heating,[1] drug delivery,[2] blood purification[3]) and diagnostic applications.[4] In particular, their utilization as contrast agents for

Abbreviations: FoV, field of view; FSE, fast spin-echo; ICP-MS, inductively coupled plasma mass spectroscopy; mGRE, multi-echo gradient-echo; RoI, region of interest; T_E, echo time; UTE, ultrashort echo time; ZTE, zero echo time.

MRI has been frequently investigated and led to several clinically approved products.[5] Due to their biocompatibility, they are an attractive alternative to gadolinium-based MRI contrast agents, which face considerable toxicity concerns.[6]

Depending on oxidation state and size, iron-based nanoparticles attain various magnetic states, ranging from paramagnetic to superparamagnetic or ferromagnetic. These characteristics can cause shortened T_1, T_2, or T_2^* relaxation times as well as phase and susceptibility changes by influencing the magnetic environment of surrounding hydrogen protons. For example, when superparamagnetic magnetic iron oxide or ferromagnetic iron nanoparticles are injected in vivo, they induce distortions of the magnetic field around them, resulting in shortening of the T_2 and T_2^* relaxation times of tissues in which they accumulate. The reduction of T_2^* relaxation time provides a negative enhancement, resulting in the generation of a hypointense signal that appears dark on T_2^*-weighted images.[7] Iron-based nanoparticles not only impact on T_2/T_2^* relaxation times but also reduce the longitudinal relaxation time T_1, which may result in signal increase for low concentrations.

Research in the field has so far focused predominantly on the development of novel iron-based nanoparticles with optimized magnetic characteristics. While the advancement in this regard has started to stagnate, the understanding of the biodistribution of nanostructures in general is still limited.[8] This is surprising, as the low targeting efficiencies of nanoparticles are frequently considered as the bottleneck in the development of highly efficient diagnostic and therapeutic nanosystems.[9]

Radiology and especially MRI provide promising approaches to this issue. Iron deposits, eg as a consequence of hemochromatosis, are routinely assessed via exponentially decaying signals seen in multi-echo gradient-echo sequence (mGRE) MRI.[10,11] The measurement of T_2^* transverse relaxation times is widely recognized as the primary approach to quantify the distribution and concentration of iron-based deposits in the liver.[12] Hence, such methods are in principle well suited for the biodistribution analysis of iron-based nanoparticles, although their concentrations are typically lower.

Standard MR sequences offer echo times (T_E) in the range of a few milliseconds for spin-echo sequences and down to 1 ms for gradient-echo sequences. Signals arising from tissues with a very short T_2, well below 1 ms, are therefore not visible using standard sequences, as the signal has already decayed by the time of acquisition. In the image, these tissues appear dark and indistinguishable from air cavities or noise. With conventional MRI sequences, such as fast spin-echo sequences (FSE), which use T_E values longer than 1 ms, there is no possibility to encode the decaying signal of short- and ultrashort-T_2/T_2^* tissues before it has reached zero or near zero. A short T_2 can usually be found in tissue with strong couplings of solid materials such as teeth, ligaments, tendons, and bones in the human body.

Moreover, iron content quantification via R_2^*-MRI using mGRE imaging in general is compromised towards high iron concentrations or at higher fields due to ultrafast signal decay.[13,14] In the lung, mGRE of the pulmonary parenchyma is especially challenging since it is hampered by multiple challenges, primarily related to (1) patient respiratory- and circulation-related motion, (2) low proton density, and (3) extremely fast signal decay caused by microscopic magnetic field inhomogeneities between alveoli and air. The aforementioned limitations of mGRE-based iron concentration estimation could be overcome by using ultrashort-echo-time (UTE) imaging.[15,16] UTE imaging allows for very short delays (≤100 μs) between signal excitation and data acquisition, thereby enabling the detection of tissues with very short transverse relaxation times, such as cortical bone[17,18] and lungs.[19,20]

This study aims to demonstrate the feasibility of UTE-based T_2^* mapping for semi-quantitative measurement of iron concentration in liver, spleen, and lung of mice injected with nanoparticles.

2 | MATERIAL AND METHODS

2.1 | Study design

The study was approved by the local veterinary office of the canton of Zurich. C57BL/6 mice (8-10 weeks old, female) were injected with 200 μL of non-oxidic Fe or $AuFeO_x$ nanoparticle dispersion at two different concentrations (1 mg/mL (low) and 3 mg/mL (high)) in the tail vein, resulting in a dose of 200 or 600 μg per mouse, respectively. For each condition, four mice were injected and two untreated mice served as control (no sham injection). Additionally, nanoparticle distribution was also studied in two tumor-bearing mice, where liver metastases were induced using a well established protocol.[21] Finally, to investigate potential alterations in biodistribution due to knocked-down macrophages, nanoparticle distributions were investigated in wild type mice compared with macrophage-depleted mice. All MRI measurements of the above mice were performed 24 h after nanoparticle injection. In the sequence optimization (13 additional mice), a set of echo times for the UTE sequence was initially tested (T_E = 20 μs, 100 μs, 500 μs, 1,500 μs). In the final protocol, five different echo times were used (see below).

2.2 | Animal surgery

Animal surgery was carried out as previously described.[21] Interventions were performed by a surgeon with extensive experience in experimental microsurgery. Isoflurane inhalation (Attane, Minrad I, Buffalo, NY) 2-3% mixed with pure oxygen was used for anesthesia induction; intraoperative

analgesia was administered via subcutaneous application of buprenorphine (0.1 mg/kg body weight). For metastasis induction, median laparotomy was performed after fixation of the animal with tape on a heating pad. The liver was mobilized by cutting the falciform ligament and the membrane between caudate and left lateral lobe with microsurgical scissors. After display of the portal vein, 1×10^5 MC-38 tumor cells, prepared in 100 μL PBS (phosphate buffered saline), were injected intraportally with a 29-gauge insulin syringe. The needle was then removed and hemostasis achieved by gentle pressure with cotton swabs and application of small pieces of TachoSil (Baxter, Deerfield, IL), if necessary. The abdomen was closed with two layered continuous sutures with 5-0 prolene. Mice recovered on a warmed heating pad, and food and water were provided 1 h after the operation. Postoperative analgesia with buprenorphine was administered via drinking water for three days. Animals underwent MRI one week after liver tumor induction. Macrophages were depleted using anti-CFSR1 antibody (300 μg/mouse; Bio X Cell, Lebanon, NH) 12 h prior to nanoparticle injection. Mice were sacrificed after the MRI examination.

2.3 | Nanoparticle production

Dry and scalable flame spray pyrolysis was used for the nanoparticle synthesis, as described elsewhere in detail for $AuFeO_x$[22] and Fe.[23] The non-oxidic iron nanoparticles consist of iron carbide (Fe_3C) and are encapsulated by a thin carbon shell of a few nanometers. The $AuFeO_x$ nanoparticles consist of a Janus-like Au/Fe_2O_3 core structure (30 at.% Fe = $mol_{Fe}/[mol_{Fe} + mol_{Au}]$) hermetically covered by an inert SiO_2 coating (13 wt% $SiO_2 = m_{SiO2}/(m_{SiO2} + m_{Au} + m_{Fe2O3})$. The as-prepared nanoparticles were surface functionalized with polyethylene glycol via silane chemistry. Typically, 10 mg $AuFeO_x$ nanoparticles were dispersed in 17.5 mL ethanol (puriss p.a., Sigma Aldrich, MO, USA) via strong ultrasonication (Sonics Vibra-Cell, Sonics & Materials, Inc., Newtown, CT, USA, 8 kJ, power 90%, pulse on/off 10 s/10 s) for 90 s. Thereafter, 1.25 mL NH_3 (25%, analytical reagent, Riedel-de Haen, Honeywell Specialty Chemicals, Seelze, Germany) was added and the dispersion again sonicated for 30 min. Then 50 μL APTES ((3-aminopropyl)triethoxysilane, 99%, Sigma Aldrich) was added, the reaction was started and kept at 25 °C for 1 h under shaking (800 rpm). Afterwards, the particle dispersion was washed via centrifugation (15 min, 8500 rpm) twice with ethanol and twice with ultrapure water and then dispersed in 2 mL of borax buffer to a concentration of 5 mg/mL. The resulting dispersion of amine functionalized nanoparticles was then sonicated for 30 min. Afterwards 100 mg mPEG-SC (5 k, methoxypoly(ethylene glycol) succinimidyl carbonate, Biochempeg, Watertown, MA, USA) was dissolved in 2 mL borax buffer and mixed with the freshly sonicated particle dispersion to initiate the reaction. The resulting mixture was weakly sonicated (Branson 1800 ultrasonic cleaner, Brookfield, CT, USA) for 5 min before being placed in a shaker for 24 h (25 °C, 800 rpm). Afterwards, the particles were washed via centrifugation (15 min, 8500 rpm) once in borax buffer and once in ultrapure water before storing them at 1 mg/mL in saline (0.9%) for further experiments.

2.4 | Microscopy and elemental analysis

Tissue samples were fixed in formalin and post-fixed in 0.2% glutaraldehyde. They were paraffin embedded and sectioned using standard histology sample preparation protocols established at Sophistolab (Muttenz, Switzerland). Tissue sections were hematoxylin and eosin or F4/80 stained and imaged by optical microscopy (Zeiss, Oberkochen, Germany) at different magnifications. A whole slide scanner (ScopeM, ETH Zurich) was used to obtain overview images. Inductively coupled plasma spectrometry was used for iron and gold quantification in tissue after digestion using an Agilent 7900 (Santa Clara, CA, USA).

2.5 | MRI

All MRI examinations were carried out in a Bruker 4.7 T BioSpec 47/40 (Bruker BioSpin, Ettlingen, Germany) equipped with a circular polarized ^1H mouse whole body transmit-receive RF coil. The animal bed was equipped with a pad with continuous warm water flow supply to keep the mouse warm. Mice were anesthetized during MRI with 0.6% isoflurane (1-chlor-2,2,2-trifluorethyl-difluoromethylether) (Attane; Minrad I, Buffalo, NY) mixed with 100% oxygen. The animal's eyes were protected from drying by applying sterile ophthalmic ointment (Vit. A Crème, Bausch & Lomb Swiss, Steinhausen, Switzerland). A gradient-echo localizer was applied in three spatial directions to provide anatomical overview. A transverse oriented T2w FSE sequence (T_R 4410 ms/first echo 15 ms; effective T_E 45 ms; echo train length 8; matrix 384 × 384; field of view (FoV) 45 × 45 mm; slice thickness 1 mm, three averages) was used to depict organ morphology. For visualization of fast relaxing tissue and for relaxation measurements, a three-dimensional UTE sequence was applied with five subsequent acquisitions with T_E = 100 μs, 500 μs, 1500 μs, 3000 μs, and 5000 μs, respectively. For spin excitation, a non-selective RF block pulse of 20 μs duration was applied. Further protocol parameters of the UTE sequence were the following: repetition time T_R = 8 ms; matrix 128 × 128 × 128; FoV 45 × 45 × 45 mm^3; spatial resolution 0.35 × 0.35 × 0.35 mm^3; flip angle 18.9°; one averages; acquisition time 6 m 50 s for each echo time. The standard reconstruction algorithm of the Bruker UTE3D sequence was applied for image reconstruction.

2.6 | Data analysis

Data analysis was performed on a stand-alone personal computer using custom-made routines in the MATLAB programming language (MathWorks, Natwick, MA). Signal intensity curves and parametrical maps of T_2* relaxation times were computed by mono-exponential fitting. A nonlinear least square fit to the signal intensities was performed based on the Levenberg-Marquardt algorithm using the following equation:

$$S(TE_i) = S(0) * e^{-\frac{TE_i}{T2*}} + N$$

with S denoting the signal intensity, T_{Ei} meaning the different times to echo, T_2* the apparent transverse relaxation time, and N the noise (three variables fitted).

For signal intensity curves, a polygonal region of interest (RoI) was manually placed to encompass as much of the investigated organ tissue as possible. RoI analysis was performed three times in each mouse in three different slices. In the lungs, the subpleural area was chosen to avoid signal contamination from large vessels. Moreover, RoI measurements were made on both sides of the lung. In liver parenchyma, RoI measurements were made three times in the lower and upper parts of the liver.

For statistical analysis, mean values and standard deviations were computed. The Kruskal-Wallis test was used to test for significance between two groups. P values less than 0.05 were considered statistically significant. All statistical analyses were performed using commercially available software (SPSS, Release 17.0, Chicago, IL).

3 | RESULTS

3.1 | Qualitative assessment of image quality

FSE sequences with T_2-weighted contrast (T_E 45 ms) and UTE sequences (T_E between 100 μs and 5000 μs) were acquired. Representative images are shown in Figure 1. In mice without nanoparticle injection, the FSE sequences show intermediate signal intensity of the liver, allowing for

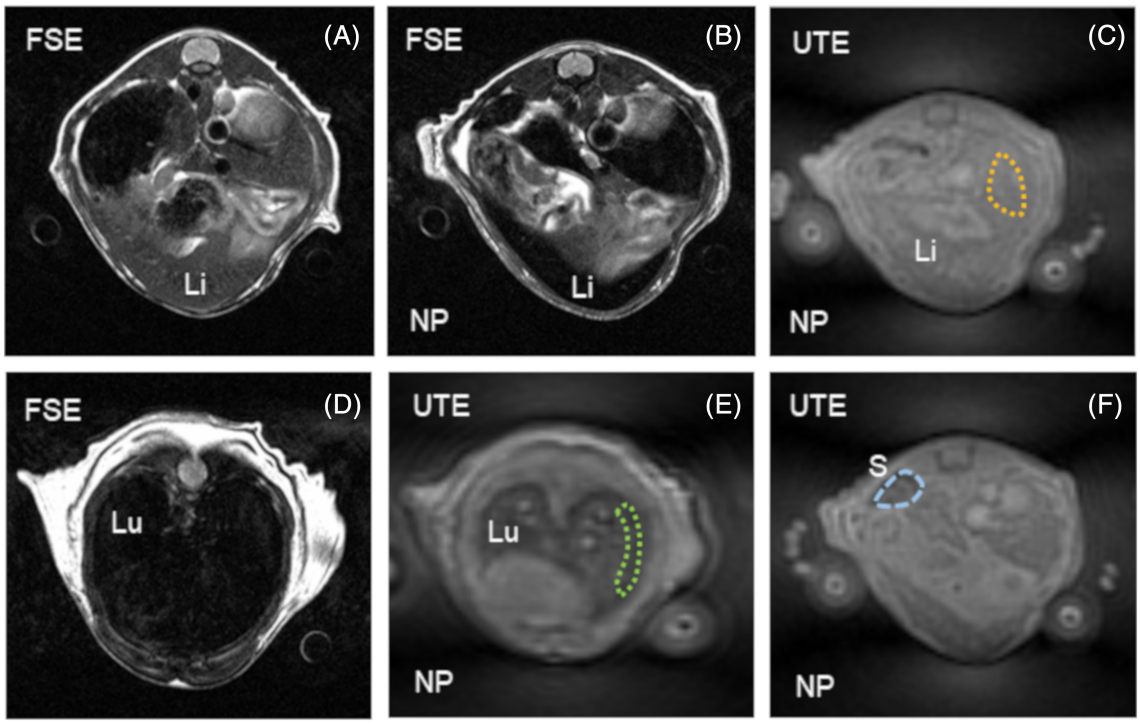

FIGURE 1 FSE (T_E = 45 ms) (A, B, D) and UTE sequence (T_E = 100 μs) (C, E, F) MR images of metastasis-free mice with and without administration of Fe nanoparticles (low dose). A-C, The liver parenchyma, which darkens due to a complete signal loss caused by the accumulated Fe nanoparticles. D, E, Images of the lung. No signal can be measured in lung parenchyma using an FSE sequence due to the fast signal decay caused by microscopic magnetic field inhomogeneities. Using a UTE sequence with echo time T_E = 100 μs, signal above the background noise level can be measured in iron-loaded liver, spleen, and lung parenchyma. Typical RoI measurements for computation of signal curves are indicated by the dashed lines. Li indicates liver, Lu lung, and S spleen. NP, nanoparticles

assessment of liver parenchyma. In mice treated with Fe nanoparticles, a complete signal loss to background noise can be observed in liver parenchyma caused by the magnetic field inhomogeneities induced by nanoparticles. In the lungs, regardless of whether nanoparticles have been applied or not, a complete signal loss is observed in the FSE sequence. Applying UTE sequences, in iron-loaded liver, iron-loaded spleen, and lungs, signal above the noise level can be observed. Visually on MR images iron deposition was only observable in liver and spleen parenchyma, and from image impression alone nanoparticle deposition in the lung was not detectable. Liver metastases were detectable in both FSE and UTE sequences (Figure 2). However, in the liver loaded with Fe nanoparticles the normal parenchyma could not be assessed due to signal loss, whereas in UTE sequences both liver metastases and iron-loaded liver parenchyma were visible. No uptake of nanoparticles was seen in the metastases.

3.2 | Signal intensity curves

Example T_2^* signal intensity curves are shown in Figure 3. From the curves it can be seen that an excellent curve fitting based on the five signal intensities of different echo times between 100 μs and 5,000 μs was possible in untreated mice as well as for both nanoparticle compositions and for both injected numbers of nanoparticles in liver, lung and spleen. A sequence with even shorter echo time of 20 μs resulted in worse signal-curves due to a signal loss at this echo time compared with the later echo at 100 μs, which may be due to hardware limits of the ADC converter. No reliable signal curves could be computed from tissues with T_2^* relaxation times longer than the liver (eg muscle tissue). Investigation of such tissues would have required the inclusion of even longer echo times in the MRI protocol. In contrast, signal curves with suitable quality could be obtained from the lung tissue in all mice (treated and untreated).

3.3 | Quantitative T_2^* transverse relaxation times

An overview of the measured T_2^* values is visualized in Figure 4; numeric mean values and standard deviations are provided in Table 1. No statistical difference was found between the left and right sides of the lungs; therefore, T_2^* values from the two sides were pooled. Liver T_2^* values were shorter close to the diaphragm compared with the more caudal parts of the liver (data not shown), which is most likely due to macroscopic magnetic field inhomogeneities close to the diaphragm (tissue-air interface). Dependent on the nanoparticle type and dose, a reduction of T_2^* values can be seen in liver, spleen, and lung tissue. Macrophage depletion was performed to increase the nanoparticle deposition in the lungs, resulting in

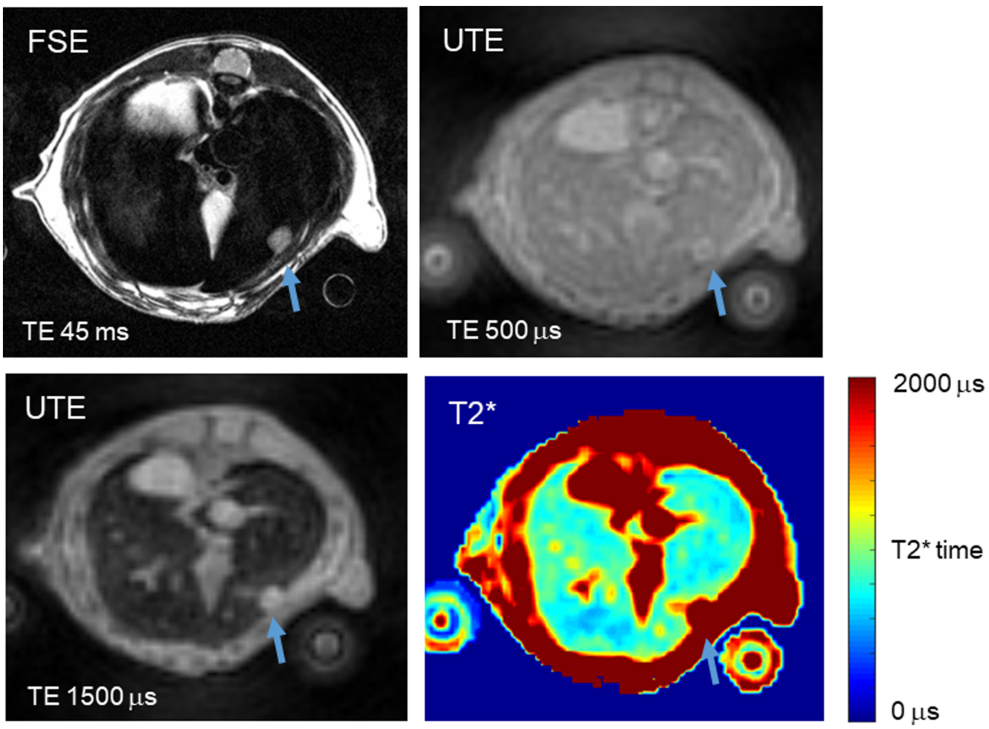

FIGURE 2 FSE and UTE sequence MRIs of mouse liver metastases after Fe nanoparticle administration (low dose). A T_2 hyperintense metastasis (arrow) can be seen in the FSE image with complete signal loss of the surrounding iron-loaded liver parenchyma. In the UTE sequences, both liver parenchyma and metastasis are clearly visible using T_E of 500 μs and 1500 μs, respectively. In the T_2^* map, the metastases show notably longer T_2^* relaxation time compared with liver parenchyma loaded with nanoparticles

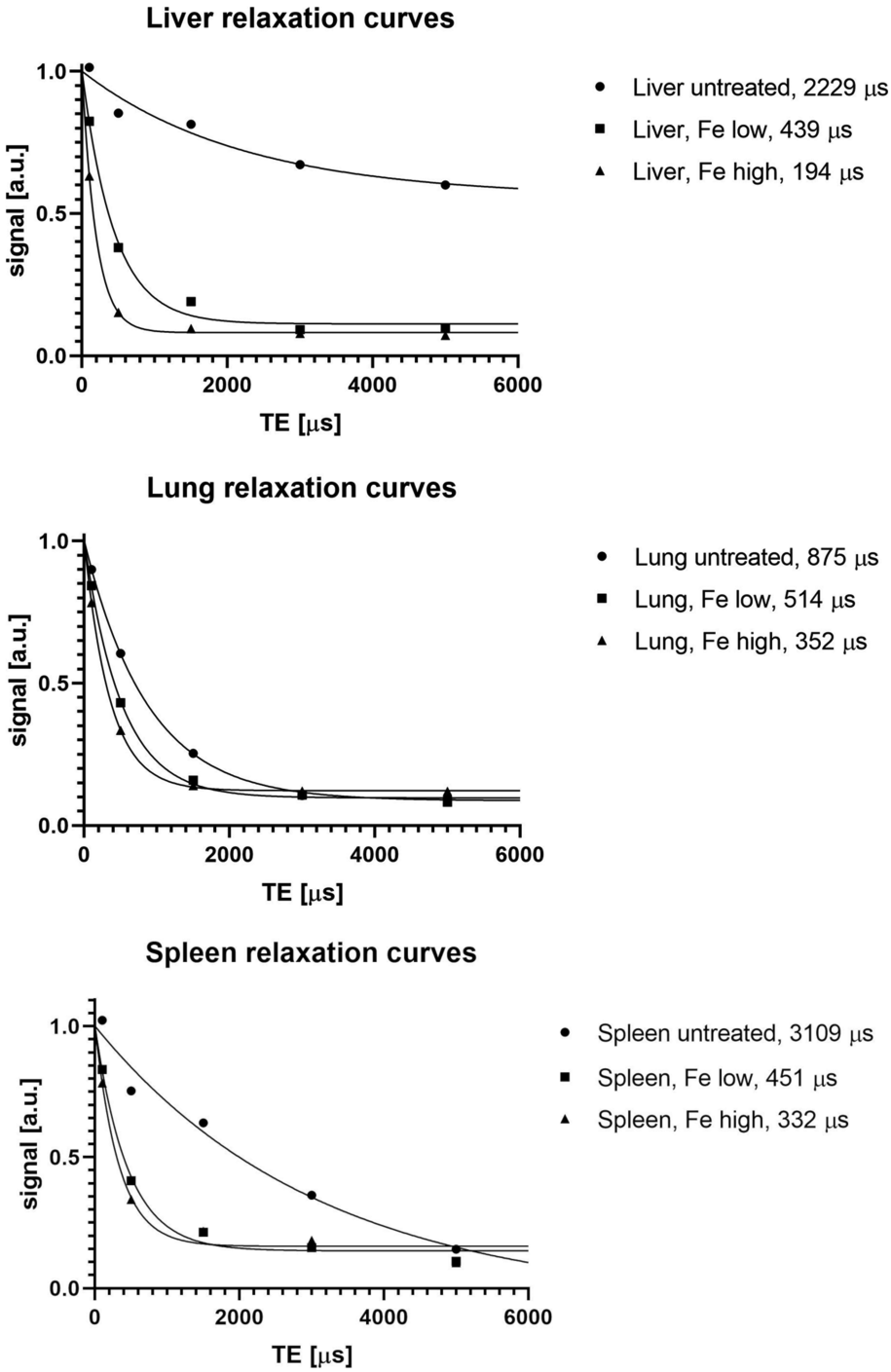

FIGURE 3 T_2^* signal relaxation curves (measurement points and corresponding mono-exponential fits) for liver (top), lung (middle) and spleen (bottom) parenchyma. The computed transverse relaxation times are shown in the legends

a similar reduction of T_2^* time with the low number of Fe-based nanoparticles in the lung as compared with the high number of nanoparticles without macrophage depletion. In some of theT_2^* values of Figure 4, a relatively large error bar can be seen, which may be due to inaccurate T_2^* quantification in tissues with long transverse relaxation time, small size of the evaluated organ or incomplete injection of nanoparticles in the tail vein.

3.4 | Parametrical T_2^* maps

T_2^* maps were calculated in a pixel-by-pixel manner; example images are displayed in Figures 5 and 6. From the generated T_2^* maps with good image quality, it can be seen that the curve fit is stable enough to allow pixel-wise evaluation.

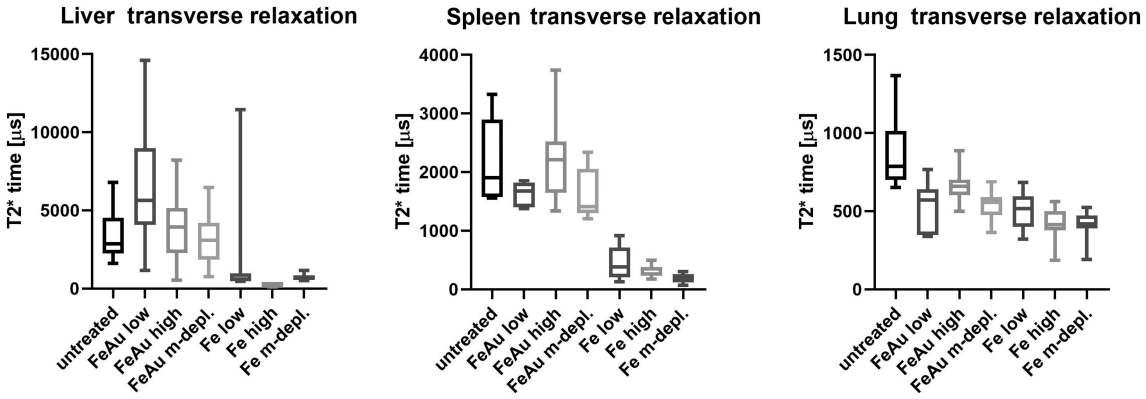

FIGURE 4 Mean and standard deviations for T_2* transverse relaxation times of liver, spleen, and lung for untreated mice, mice injected with $AuFeO_x$ or Fe nanoparticles in high and low concentrations, and mice treated by macrophage depletion before injection of low concentrations of $AuFeO_x$ or Fe nanoparticles. It can be seen that Fe nanoparticles result in stronger reduction of transverse relaxation time compared with $AuFeO_x$ nanoparticles, and the higher number of nanoparticles results in stronger reduction of T_2*. In the liver, an effect of Fe nanoparticle deposition can clearly be observed. Macrophage depletion causes a reduction of T_2* in the lung with low concentration similar to high concentration without macrophage depletion, which may be attributed to higher nanoparticle deposition in the lung due to lower accumulation in liver macrophages

TABLE 1 Mean T_2* relaxation times and standard deviations measured in the liver, kidney, and lung after application of different nanoparticle types and amounts

T_2* relaxation times [µs]			
Treatment	**Liver**	**Spleen**	**Lung**
Untreated	3418 ± 1535	2170 ± 728	861 ± 208
$AuFeO_x$ low	6438 ± 4193* ($p = 0.04$)	1634 ± 202 ($p = 0.26$)	527 ± 153* ($p < 0.01$)
$AuFeO_x$ high	3836 ± 2024 ($p = 0.50$)	2276 ± 686 ($p = 0.93$)	663 ± 101* ($p < 0.01$)
$AuFeO_x$ m-depl.	3118 ± 1521 ($p = 0.68$)	1594 ± 426* ($p = 0.04$)	539 ± 84* ($p < 0.01$)
Fe low	1771 ± 2729* ($p < 0.01$)	453 ± 280* ($p < 0.01$)	507 ± 106* ($p < 0.01$)
Fe high	228 ± 67* ($p < 0.01$)	299 ± 97* ($p < 0.01$)	413 ± 99* ($p < 0.01$)
Fe m-depl.	720 ± 173* ($p < 0.01$)	193 ± 78* ($p < 0.01$)	409 ± 89* ($p < 0.01$)
Mean RoI size [voxels]	93 ± 45	40 ± 17	44 ± 18

*Statistically significant versus untreated.

3.5 | Ex vivo characterization of the nanoparticle content in tissues

After mouse sacrifice, liver, spleen, and lungs were harvested and analyzed using histology, including macrophage staining with F4/80antibodies. Additional metal quantification was performed using inductively coupled plasma mass spectroscopy (ICP-MS). Observation of F4/80 antibody-stained sections shows the presence of black deposits in macrophages in the organs from the mice exposed to both magnetic nanoparticles, with a dose effect Figure 7). These black spots can then be related to the presence of nanoparticles, and thus confirm the presence of the Fe and $AuFeO_x$ particles in the liver and the spleen. In contrast, no differences have been observed between the lungs from the control and nanoparticle-exposed mice. This indicates that UTE sequences can potentially detect nanoparticle deposits with improved sensitivity compared with histology alone. To quantify the amount of metal, ICP-MS of liver and spleen tissue was used in three healthy mice, showing first the presence of gold only in the tissues exposed to $AuFeO_x$ nanoparticles, and second an increase of the amount of iron above the endogenous level after injection of both types of nanoparticle (Figure 8).

4 | DISCUSSION

In this study we utilize UTE imaging to better visualize typically MRI invisible organs with a short T_2*, such as lungs, and liver after application of iron-based nanoparticles providing an alternative method for investigating the biodistribution of nanoparticles, as seen in our case with an Fe nanoparticle loaded tumor-containing liver and lung. The sensitivity for the detection of magnetic nanoparticles as molecular imaging probes is

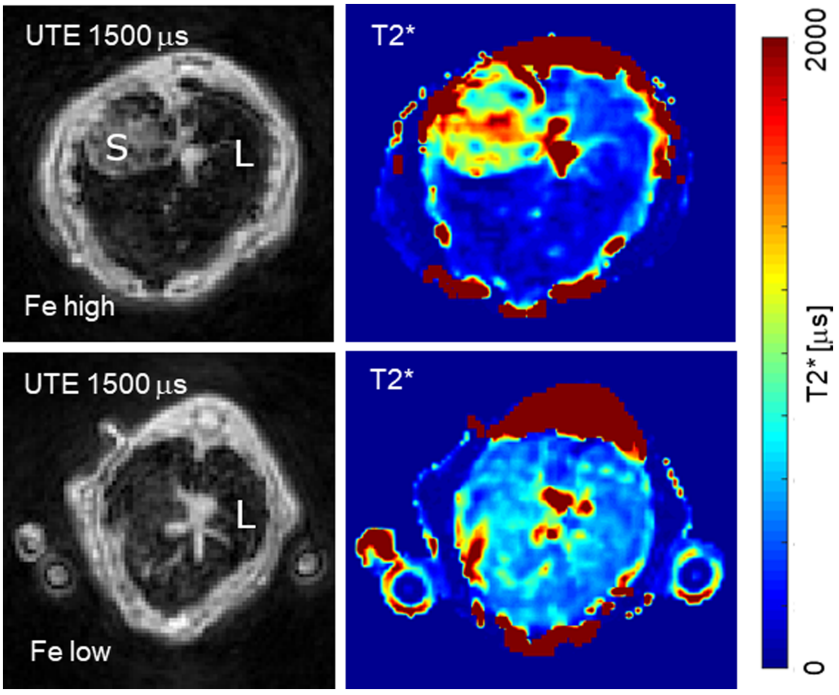

FIGURE 5 UTE images (left) and corresponding T_2^* parametrical maps (right) of the liver for high (top) and low (bottom) numbers of injected Fe nanoparticles. L, liver; S, stomach

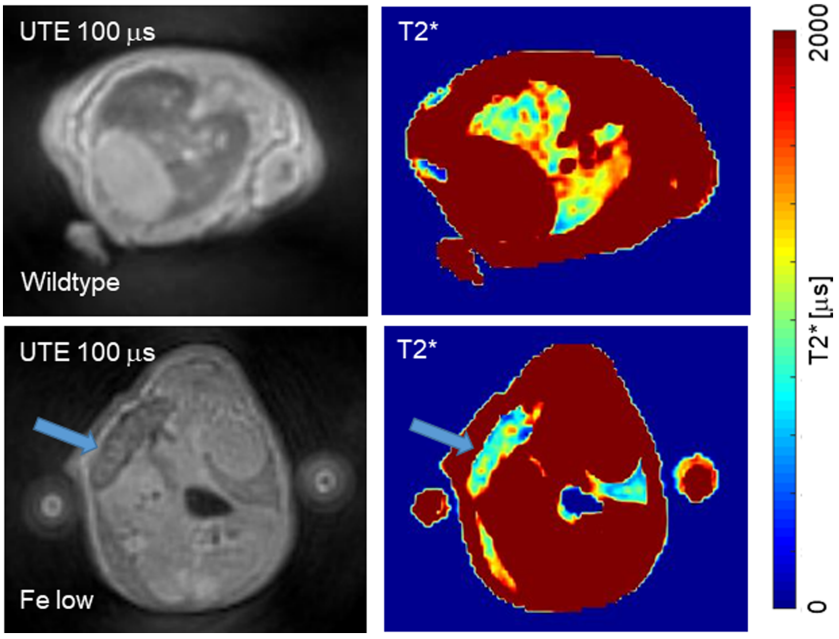

FIGURE 6 UTE images (left) and corresponding T_2^* parametrical maps (right) of the basis of the lungs without injected nanoparticles and of the spleen (blue arrow) with low number of injected Fe nanoparticles

enhanced due to the increased signal yield, and a semi-quantitative measurement of nanoparticle concentration is provided by computation of T_2^*.

Using FSE, we observed complete signal loss in the liver parenchyma after nanoparticle injection and deposition. We did not find any signal in lungs with FSE after nanoparticle deposition due to fast signal decay caused by microscopic magnetic field inhomogeneities owing to tissue-air interfaces in the alveoli of lungs. Using a UTE sequence with echo time $T_E = 100$ µs, signals above the background noise level can be measured in Fe nanoparticle loaded livers with differentiated metastasis, spleen, and lung parenchyma.

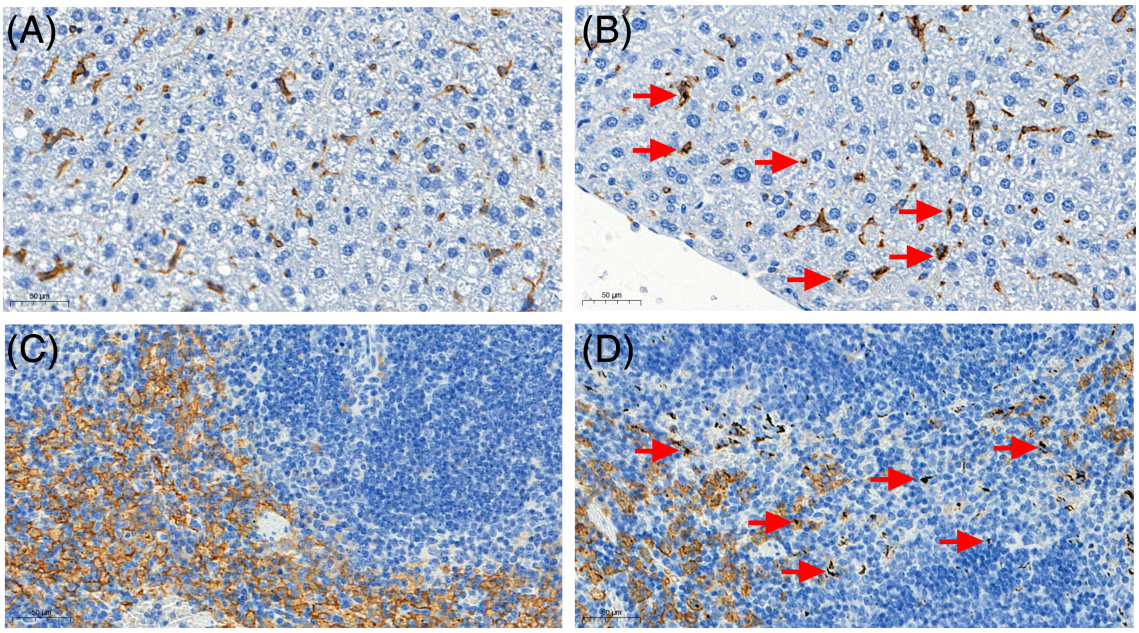

FIGURE 7 Imaging of histology sections of liver (A, B) and spleen (C, D) after tissue staining with F4/80 antibody. Micrographs in A and C present sections of organs harvested from vehicle injected animals (A, C); B and D display micrographs of animals injected with a high dose of Fe (B, D). In the latter, red arrows indicate the presence of characteristic black depositions. Scale bars: 50 μm

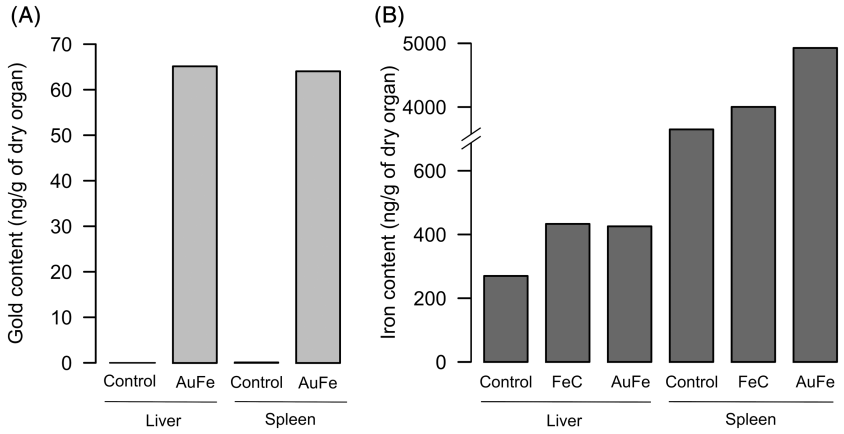

FIGURE 8 Quantification of the iron (and gold) content in the livers and spleens from mice injected with vehicle solution, low dose of Fe nanoparticles or low dose of $AuFeO_x$ nanoparticles. Results displayed for one mouse per condition

It is known that tissues with low background signals and nanoparticle induced susceptibility artifacts require fast signal acquisition starting immediately after the RF excitation. In UTE pulse sequences, the RF excitation is performed before gradients are ramped up and data acquisition begins after a short, non-negligible delay time. Data acquisition occurs while the readout gradient is being ramped on. Since the readout gradients are turned on at the beginning of data acquisition, the sampling pattern of *k*-space is radial, filled from the center out, and is nonlinear in time. UTE can be applied for 2D imaging,[24,25] with a slice selective gradient during the RF pulse while encoding in two directions, or for 3D imaging, without any slice selective gradients and encoding in all three directions. Slice selective 2D radial acquisition may be used to image brain tissue,[26] cortical bone,[27,28] and tendons.[29] An acquisition-weighted stack of spirals sequence has been proposed for high-resolution 3D UTE imaging.[30] Typically, radial trajectories are used, although other center-out trajectories such as spirals,[31] twisted projections,[32] or cones[33] are also feasible. However, it must be pointed out that center-out techniques for lung imaging are limited by the required rather long readout.

UTE shares with the other radial sampling techniques the advantage of being less sensitive to motion artifacts compared with cartesian sampling.[34] One challenge of the UTE sequence is that acquiring data during gradient ramping can lead to major image distortions originating from eddy currents and time delays within the gradient system. Zero-T_E imaging may overcome this problem. A disadvantage of UTE imaging is that it typically requires a relatively long scan time compared with conventional T_2^*-weighted GRE. However, UTE imaging is advantageous and

potentially more sensitive compared with T_2 and T_2^* imaging using standard sequences when nanoparticle concentrations are high in the tissue, but may not be beneficial when the tissue nanoparticle concentration is low. In particular, in tissues with long relaxation time inaccuracies in T_2^* quantifications may occur with UTE sequences, as the curve shape and the noise level cannot reliably be estimated.

Zero echo-time (ZTE) or UTE pulse sequences use specialized acquisition and reconstruction techniques to enable detection of ultrashort-T_2 components in vivo, and rely on beginning data acquisition as soon as possible after completion of the RF pulses.[35] Radial imaging, as in UTE and ZTE, is particularly robust to movement artifacts. A certain amount of image blurring must nevertheless be expected if motion is present during the acquisition. Thus, the need of the day is for techniques such as UTE and ZTE, which are able to compensate for motion, resulting in the best image quality possible. Moreover, such techniques can be useful to determine the influence of motion over parameter quantification in motion corrupted datasets.

Different tissues and organs have different T_2^* values, and the different statuses of the same tissues and organs also have different T_2^* values. Thus, the T_2^* value has the potential to reflect a change in the biochemical components of the counterpart and may be used for the early diagnosis and quantitative description of some diseases, eg to detect and quantify excess iron deposition in various organs such as the liver, heart, spleen, pancreas, and pituitary gland.[36] In T_2^*-weighted sequences, the lesion, structures, or areas of dephasing are shown as dark areas, leading to their detection or characterization.[37] The T_2^*-based contrast mechanism is also used in other MR applications such as susceptibility weighted imaging, MR perfusion imaging, functional MRI, and iron overload imaging.[38] Iron overload can be caused by disorders of iron absorption, such as hereditary hemochromatosis and thalassemia intermedia, defects in heme metabolism, or long-term transfusion therapy.[39,40]

Iron nanoparticles, as magnetically active agents, primarily shorten transverse relaxation times T_2 and T_2^*, which leads to prominent signal decrease or "negative contrast" of targeted tissue on T_2- and T_2^*-weighted images. UTE imaging enables capturing signal of the shortened T_2 and T_2^*, allowing for obtaining signal from tissues with rapidly decaying transverse relaxation, as observed in the current study. Here we saw that Fe nanoparticles result in stronger reduction of transverse relaxation time compared with $AuFeO_x$ nanoparticles. This can be explained by the higher saturation magnetization of the Fe nanoparticles (140 emu/g)[41] compared with the $AuFeO_x$ system (43.5 emu/g).[22] Also, as expected, a higher concentration of nanoparticles results in stronger reduction of T_2^*. In the liver, an effect of nanoparticle deposition can clearly be observed. Interestingly a reduction of T_2^* for lung parenchyma in vivo after nanoparticle deposition has been shown for the very first time here in this study.

The lung parenchyma properties that are important in the context of its visualization with MRI are its low density and the susceptibility differences between tissue and air. The tissue density in a healthy human lung is around 0.1 g/cm^3,[42] which is about 1/10 that of other tissues. As the MR signal is directly proportional to the tissue proton density, the MR signal arising from the lung is 10 times weaker than that of other tissues, even prior to any relaxation. The inherently low signal to noise ratio (SNR) is one of the main limitations that makes structural proton MRI of the lung challenging, particularly when acquisition times must be within reasonable limits and high spatial and/or temporal resolution is required.[43] The second important property is the high number of tissue-air interfaces in the lung. Oxygen present in the air is paramagnetic and lung tissue is diamagnetic, leading to a magnetic susceptibility difference at lung-air interfaces. Since between two areas of different susceptibility there exists a small static magnetic field, this results in a highly inhomogeneous local magnetic field on a spatial scale smaller than the size of a typical voxel. This leads to a rapid signal dephasing in gradient-echo imaging, and thus to short T_2^*. Thus, gradient-echo MRI of lung parenchyma becomes highly challenging and requires pulse sequences with peculiarly low T_E. Moreover, continuous motion is present in the thoracic and abdominal area, due to the presence of respiratory movements and the heartbeat. This requires countermeasures for avoiding artifacts and image blurring, which may happen when these movements occur on a time scale shorter than the acquisition time of the image.[44]

The T_2^* relaxation time of tissues is dependent on many parameters, eg the voxel size, the voxel geometry, the field strength, the number of echoes, the distribution of the measured echoes, and the technique for calculating T_2^* (fitting algorithm). In general, the larger the voxel size and the higher the field strength, the faster the transverse signal decay. The treatment of noise can strongly influence the calculated T_2^* depending on whether a fixed or variable noise is used in the fitting algorithm. Using a 3D UTE sequence at 4.7 T with an isotropic spatial of $0.35 \times 0.35 \times 0.35$ mm^3 with five different echo times and variable fitting of noise, we measured a T_2^* of normal lung of 860 μs. Olsson et al[45] at the same field strength used a larger voxel size of $0.31 \times 0.31 \times 1.56$ mm^3, only two echo times, and an algorithm with fixed noise measuring 460 μs. Guo et al[46] used 7 T field strength, a spatial resolution of $0.47 \times 0.47 \times 0.47$ mm^3 and six different echo times, measuring a T_2^* of 395 μs. Balasch[47] measured 200 μs at 11.7 T using a spatial resolution of $0.2 \times 0.2 \times 0.2$ mm^3, 10 echo times, and local noise measurement.

Our study had several limitations. First, only a small number of animals have been used, with four mice dedicated to each concentration and nanoparticle type. Due to rules of animal welfare, the 3R principles (reduce, replace, refine) must be applied, and we believe that with the applied study design we were able to demonstrate the main aims of our study. However, we cannot exclude that using more animals in each branch of the study would have been achieved even better results. Second, after UTE protocol optimization and finalizing the post-processing routines, we cannot exclude that even better settings for both the UTE sequence (with less background blurring) and the post-processing algorithms could have been found. However, the final settings used in this study were shown to provide consistent and reliable results. Third, only five different echo times of the UTE sequence have been acquired, which is due to the approved animal protocol restricting the possible time of the MRI examination protocol due to cooling of the animals. Fourth, all experiments have been carried out at 4.7 T, and potentially better image quality and higher quantification accuracy could have been achieved with higher field strength or other types of improved hardware. In particular, it would have been desirable to acquire signal at even shorter echo time such as 100 μs, which was not possible with our hardware set-up. A shorter

transmit/receive switch might be a solution, as described by Sheth et al.[48] Fifth, for accurate iron quantification, a calibration curve would be needed correlating the tissue iron content to the corresponding T_2^*. Due to differences in the intrinsic tissue-specific T_2^* relaxation times, a separate curve would be required for each organ to be evaluated. In the current study, we abstained from exact calibration of the iron-T_2^* curves, as this would require a large number of animals injected with different numbers of nanoparticles. Finally, a technique called quantitative susceptibility mapping was recently described to be combined with UTE imaging (UTE-QSM), which might be superior for iron quantification compared with T_2^* mapping.

In conclusion, we have demonstrated that UTE imaging can be used for obtaining increased signal in tissues loaded with iron-based nanoparticles and consequently short transverse relaxation time. In particular, detection of nanoparticles loaded in lung parenchyma becomes feasible. A semi-quantitative measurement of nanoparticle concentrations can be obtained by calculating T_2^* from UTE imaging of different echo times.

ACKNOWLEDGEMENTS

Open Access Funding provided by Universitat Zurich.

ORCID

Andreas Boss https://orcid.org/0000-0003-1091-5434

REFERENCES

1. Chang D, Lim M, Goos J, et al. Biologically targeted magnetic hyperthermia: potential and limitations. *Front Pharmacol*. 2018;9:831.
2. Price PM, Mahmoud WE, Al-Ghamdi AA, Bronstein LM. Magnetic drug delivery: where the field is going. *Front Chem*. 2018;6:619.
3. Herrmann IK, Schlegel AA, Graf R, Stark WJ, Beck-Schimmer B. Magnetic separation-based blood purification: a promising new approach for the removal of disease-causing compounds? *J Nanobiotechnol*. 2015;13(49).
4. Paliwal SR, Kenwat R, Maiti S, Paliwal R. Nanotheranostics for cancer therapy and detection: state of the art. *Curr Pharm Des*. 2020;26(42):5503-5517.
5. Gandhi SN, Brown MA, Wong JG, Aguirre DA, Sirlin CB. MR contrast agents for liver imaging: what, when, how. *Radiographics*. 2006;26(6):1621-1636.
6. Rudnick MR, Wahba IM, Leonberg-Yoo AK, Miskulin D, Litt HI. Risks and options with gadolinium-based contrast agents in patients with CKD: a review. *Am J Kidney Dis*. 2021;77(4):517-528.
7. Sosnovik DE, Nahrendorf M, Weissleder R. Magnetic nanoparticles for MR imaging: agents, techniques and cardiovascular applications. *Basic Res Cardiol*. 2008;103(2):122-130.
8. Conde J, Dias JT, Grazu V, Moros M, Baptista PV, de la Fuente JM. Revisiting 30 years of biofunctionalization and surface chemistry of inorganic nanoparticles for nanomedicine. *Front Chem*. 2014;2:48.
9. Despotopoulou D, Lagopati N, Pispas S, Gazouli M, Demetzos C, Pippa N. The technology of transdermal delivery nanosystems: from design and development to preclinical studies. *Int J Pharm*. 2022;611:121290.
10. Alustiza Echeverria JM, Castiella A, Emparanza JI. Quantification of iron concentration in the liver by MRI. *Insights Imaging*. 2012;3(2):173-180.
11. Henninger B, Alustiza J, Garbowski M, Gandon Y. Practical guide to quantification of hepatic iron with MRI. *Eur Radiol*. 2020;30(1):383-393.
12. Hitti E, Eliat PA, Abgueguen E, et al. MRI quantification of splenic iron concentration in mouse. *J Magn Reson Imaging*. 2010;32(3):639-646.
13. Hankins JS, McCarville MB, Loeffler RB, et al. R_2^* magnetic resonance imaging of the liver in patients with iron overload. *Blood*. 2009;113(20):4853-4855.
14. Henninger B, Zoller H, Rauch S, et al. R_2^* relaxometry for the quantification of hepatic iron overload: biopsy-based calibration and comparison with the literature. *Rofo*. 2015;187(6):472-479.
15. Robson MD, Gatehouse PD, Bydder M, Bydder GM. Magnetic resonance: an introduction to ultrashort TE (UTE) imaging. *J Comput Assist Tomogr*. 2003;27(6):825-846.
16. Krafft AJ, Loeffler RB, Song R, et al. Quantitative ultrashort echo time imaging for assessment of massive iron overload at 1.5 and 3 Tesla. *Magn Reson Med*. 2017;78(5):1839-1851.
17. Marcon M, Keller D, Wurnig MC, et al. Separation of collagen-bound and porous bone water transverse relaxation in mice: proposal of a multi-step approach. *NMR Biomed*. 2016;29(7):866-872.
18. Marcon M, Keller D, Wurnig MC, et al. Separation of collagen-bound and porous bone-water longitudinal relaxation in mice using a segmented inversion recovery zero-echo-time sequence. *Magn Reson Med*. 2017;77(5):1909-1915.
19. Chuck NC, Boss A, Wurnig MC, Weiger M, Yamada Y, Jungraithmayr W. Ultra-short echo-time magnetic resonance imaging distinguishes ischemia/reperfusion injury from acute rejection in a mouse lung transplantation model. *Transpl Int*. 2016;29(1):108-118.
20. Jungraithmayr W, Chuck N, Frauenfelder T, Weder W, Boss A. MR imaging by using very short echo-time sequences after syngeneic lung transplantation in mice. *Radiology*. 2012;265(3):753-761.
21. Becker AS, Schneider MA, Wurnig MC, Wagner M, Clavien PA, Boss A. Radiomics of liver MRI predict metastases in mice. *Eur Radiol Exp*. 2018;2:1-11.
22. Sotiriou GA, Starsich F, Dasargyri A, et al. Photothermal killing of cancer cells by the controlled plasmonic coupling of silica-coated Au/Fe_2O_3 nanoaggregates. *Adv Funct Mater*. 2014;24(19):2818-2827.
23. Herrmann IK, Grass RN, Mazunin D, Stark WJ. Synthesis and covalent surface functionalization of nonoxidic iron core-shell nanomagnets. *Chem Mater*. 2009;21(14):3275-3281.
24. Josan S, Pauly JM, Daniel BL, Pauly KB. Double half RF pulses for reduced sensitivity to eddy currents in UTE imaging. *Magn Reson Med*. 2009;61(5):1083-1089.
25. Abe T. Half radiofrequency pulse excitation with a dedicated prescan to correct eddy current effect and gradient delay. *Med Phys*. 2013;40(3):032304.

26. Waldman A, Rees JH, Brock CS, Robson MD, Gatehouse PD, Bydder GM. MRI of the brain with ultra-short echo-time pulse sequences. *Neuroradiology*. 2003;45(12):887-892.
27. Robson MD, Bydder GM. Clinical ultrashort echo time imaging of bone and other connective tissues. *NMR Biomed*. 2006;19(7):765-780.
28. Du J, Bydder GM. Qualitative and quantitative ultrashort-TE MRI of cortical bone. *NMR Biomed*. 2013;26(5):489-506.
29. Robson MD, Benjamin M, Gishen P, Bydder GM. Magnetic resonance imaging of the Achilles tendon using ultrashort TE (UTE) pulse sequences. *Clin Radiol*. 2004;59(8):727-735.
30. Qian Y, Boada FE. Acquisition-weighted stack of spirals for fast high-resolution three-dimensional ultra-short echo time MR imaging. *Magn Reson Med*. 2008;60(1):135-145.
31. Du J, Bydder M, Takahashi AM, Chung CB. Two-dimensional ultrashort echo time imaging using a spiral trajectory. *Magn Reson Imaging*. 2008;26(3):304-312.
32. Boada FE, Gillen JS, Shen GX, Chang SY, Thulborn KR. Fast three dimensional sodium imaging. *Magn Reson Med*. 1997;37(5):706-715.
33. Gurney PT, Hargreaves BA, Nishimura DG. Design and analysis of a practical 3D cones trajectory. *Magn Reson Med*. 2006;55(3):575-582.
34. Zurek M, Johansson E, Risse F, Alamidi D, Olsson LE, Hockings PD. Accurate T_1 mapping for oxygen-enhanced MRI in the mouse lung using a segmented inversion-recovery ultrashort echo-time sequence. *Magn Reson Med*. 2014;71(6):2180-2185.
35. Weiger M, Brunner DO, Dietrich BE, Muller CF, Pruessmann KP. ZTE imaging in humans. *Magn Reson Med*. 2013;70(2):328-332.
36. Queiroz-Andrade M, Blasbalg R, Ortega CD, et al. MR imaging findings of iron overload. *Radiographics*. 2009;29(6):1575-1589.
37. Sammet CL, Swaminathan SV, Tang H, et al. Measurement and correction of stimulated echo contamination in T_2-based iron quantification. *Magn Reson Imaging*. 2013;31(5):664-668.
38. Chavhan GB, Babyn PS, Thomas B, Shroff MM, Haacke EM. Principles, techniques, and applications of T2*-based MR imaging and its special applications. *Radiographics*. 2009;29(5):1433-1449.
39. Werring DJ, Frazer DW, Coward LJ, et al. Cognitive dysfunction in patients with cerebral microbleeds on T2*-weighted gradient-echo MRI. *Brain*. 2004;127(Pt 10):2265-2275.
40. Mamisch TC, Hughes T, Mosher TJ, et al. T2 star relaxation times for assessment of articular cartilage at 3 T: a feasibility study. *Skeletal Radiol*. 2012;41(3):287-292.
41. Bradley CA, Yuhas BD, McMurdo MJ, Tilley TD. Functionalized silicone nanospheres: synthesis, transition metal immobilization, and catalytic applications. *Chem Mater*. 2009;21(1):174-185.
42. Wild JM, Marshall H, Bock M, et al. MRI of the lung (1/3): methods. *Insights Imaging*. 2012;3(4):345-353.
43. Beckmann N, Cannet C, Karmouty-Quintana H, et al. Lung MRI for experimental drug research. *Eur J Radiol*. 2007;64(3):381-396.
44. Tibiletti M, Bianchi A, Kjorstad A, Wundrak S, Stiller D, Rasche V. Respiratory self-gated 3D UTE for lung imaging in small animal MRI. *Magn Reson Med*. 2017;78(2):739-745.
45. Olsson LE, Lindahl M, Onnervik PO, et al. Measurement of MR signal and T2* in lung to characterize a tight skin mouse model of emphysema using single-point imaging. *J Magn Reson Imaging*. 2007;25(3):488-494.
46. Guo J, Cao X, Cleveland ZI, Woods JC. Murine pulmonary imaging at 7T: T_2^* and T_1 with anisotropic UTE. *Magn Reson Med*. 2018;79(4):2254-2264.
47. Balasch A, Metze P, Li H, Rottbauer W, Abaei A, Rasche V. Tiny golden angle ultrashort echo-time lung imaging in mice. *NMR Biomed*. 2021;34(11):1-14.
48. Sheth V, Shao H, Chen J, et al. Magnetic resonance imaging of myelin using ultrashort echo time (UTE) pulse sequences: phantom, specimen, volunteer and multiple sclerosis patient studies. *NeuroImage*. 2016;136:37-44.

How to cite this article: Boss A, Heeb L, Vats D, et al. Assessment of iron nanoparticle distribution in mouse models using ultrashort-echo-time MRI. *NMR in Biomedicine*. 2022;35(6):e4690. doi:10.1002/nbm.4690